Nanoscale

Tracking the Emergence of Epitaxial Metal–oxide Interfaces from Precursor Alloys

Journal:	*Nanoscale*
Manuscript ID	NR-ART-06-2021-003492.R1
Article Type:	Paper
Date Submitted by the Author:	27-Aug-2021
Complete List of Authors:	Wen, Yu; National Institute for Materials Science, In-situ Characterization Technique Development Group; University of Tsukuba, Department of Materials Science Abe, Hideki; National Institute for Materials Science, Hydrogen Production; CREST; Saitama University Mitsuishi, Kazutaka; National Institute for Materials Science, MANA Hashimoto, Ayako; National Institute for Materials Science, In-situ Characterization Technique Development; University of Tsukuba; Japan Science and Technology Agency

ARTICLE

Tracking the Emergence of Epitaxial Metal–oxide Interfaces from Precursor Alloys

Yu Wen,[a,b] Hideki Abe,[c,d] Kazutaka Mitsuishi,[a] Ayako Hashimoto *[a,b,e]

Received 00th January 20xx,
Accepted 00th January 20xx

DOI: 10.1039/x0xx00000x

Heterointerfaces with an epitaxial relationship, self-assembled nanocomposties of Pt(111)/CeO_2(111) 60°, were successfully formed by simple oxidation of Pt_5Ce alloy. Oxygen dissolution into the alloy causes spacial periodic compositonal perturbation by atomic segregation, specifically, by local diffusion of Pt and Ce atoms. A striped pattern of Pt and CeO_2 with a 4–5 nm peridicity formed through phase transformation of the Pt-rich alloy and oxidation of the Ce-rich alloy, respectively. Notably, a fully epitaxial relationship between the Pt and CeO_2 phases was observed even in the initial stage. With continued annealing, the crystals rotated into an energetically favorable orientation with respect to the remaining $(111)_{Pt}//(111)_{CeO_2}$. The alloy oxidation and its resulting nanoscale phase-separation behavior was verified in an ex-situ annealing experiment of an alloy specimen, which has been first thinned by a focused ion beam. Changing the oxygen partial pressure to the reaction interface may alter the orientation relationship between the hexagonal close-packed Pt_5Ce structure and face-centered cubic Pt/CeO_2 structure, thereby altering the growth direction of the separated phases. These findings present a pathway for the self-assembly of epitaxial Pt(111)/CeO_2(111) interface and are expected to assist the structural design of metal–oxide nanocomposites.

1. Introduction

Owing to its facile reducibility, ceria (CeO_2) is an attractive option for fuel cells and catalysts in exhaust-free vehicles.[1-3] The reduction of two Ce^{4+} cations to Ce^{3+} provides an oxygen vacancy which plays crucial roles in ionic oxygen transportation[4,5] and catalytic reactions[6,7]. Doped ceria and cerium-based hybrids with rich oxygen defects are great photocatalysts for photo-thermal reactions.[8-10] Furthermore, ceria is an important support or supported object of metal components in heterogeneous catalysis.[11-13] Strong interactions at the metal–oxide interface enable more specific performances than mono-component counterparts.[14] The interface effect between Pt and CeO_2 has been widely studied because Pt/CeO_2 catalysts are promising for water-gas shift reaction[15] and low temperature CO oxidation[16,17]. Theoretical studies[18,19] have revealed that electron transfer from Pt to CeO_2 and oxygen-vacancy formation at the interface contribute to the high catalytic activity of Pt/CeO_2. Therefore, to achieve highly active of Pt/CeO_2 catalysts, we require a rational design of the interfacial structure.

To boost the catalytic activity, researchers have developed two strategies for enhancing interactions at the Pt–CeO_2 interface. The first strategy tunes the exposed surface planes of the metal and ceria to match the oxygen vacancies density with the electronic perturbation, which typically lie in different orientations. As a model system, a Pt/CeO_2 catalyst with an epitaxial interface on the (111) plane contains a relatively high Ce^{3+} concentration[20] and facilitates charge transfer from CeO_2 to Pt[21]. The second strategy controls the configuration of Pt and CeO_2 to increase the surface area of the interface and present more active reaction sites.[22-24] Although the interface effect has been extensively engineered for fundamental study and commercial application, the preparation methods of controlled Pt/CeO_2 catalysts, such as deposition-precipitation[21,25] and electrodeposition[26,27], are generally complex and high-cost. However, the Pt_5Ce surface alloy can be post-oxidization,[28] suggesting that Pt/CeO_2 composites with an epitaxial interface can be prepared by simple oxidation of arc-melted Pt_5Ce alloy.[29]

Recently, oxidation of binary alloy has been considered as a possible route towards stable and active metal–oxide nanocomposites for catalysis.[30,31] We previously showed that the morphology of the self-assembled Pt/CeO_2 nanocomposites from Pt_5Ce alloys can be controlled to tailor the oxygen ion conductivity.[32] Moreover, various metal/oxide nanocomposites as catalysts (Ni/Nb_2O_5, Rh/Nb_2O_5, Ru/CeO_2, etc.) having superior performances were prepared via the same alloy oxidation method.[33-36] Therefore, by thoroughly understanding the oxidation process in the binary alloy, we could control the interface effect of their corresponding nanocomposites.

[a] National Institute for Materials Science, 1-2-1 Sengen, Tsukuba, Ibaraki 305-0047, Japan
[b] Graduate School of Pure and Applied Sciences, University of Tsukuba, 1-1-1 Tennodai, Tsukuba, Ibaraki 305-8577, Japan
[c] CREST, JST, 4-1-8 Honcho, Kawaguchi, Saitama 332-0012, Japan
[d] Graduate School of Science and Technology, Saitama University, 255 Shimookubo, Saitama 338-8570, Japan
[e] PREST, JST, 4-1-8 Honcho, Kawaguchi, Saitama 332-0012, Japan
† Electronic Supplementary Information (ESI) available: See DOI: 10.1039/x0xx00000x

In the present work, we track the oxidation process of Pt_5Ce alloy that leads to a self-assembled Pt/CeO_2 heterostructure, whose framework is composed by polycrystalline Pt embedded by nanocrystalline CeO_2 with epitaxial $Pt(111)/CeO_2(111)$ interface. Completely and partially oxidized samples were characterized at the atomic scale using combined high-resolution transmission electron microscopy (HRTEM) and atomic-resolution high-angle annular dark field scanning transmission electron microscopy (HAADF−STEM). The oxidation-inducing phase-separation behavior was then elucidated, and the fully epitaxial relationship of Pt and CeO_2 phases was derived from the atomic segregated alloy. The epitaxial type $(111)_{Pt}//(111)_{CeO_2}$ 60° was found at the final stage after crystal rotation. The nanoscale phase-separation behavior of the alloy was verified in an ex-situ annealing experiment on a firstly-focused ion beam (FIB)-thinned alloy.

2. Experimental

2.1 Specimen preparation

Pt_5Ce alloy was prepared by arc melting of the elemental metals in a pure argon atmosphere. Alloy powders with an average particle size of 50 um were then obtained by grinding. The alloy precursor was transferred to a reactive gas furnace (containing mixed CO and O_2 at a molecular ratio of 2:1) for phase separation. The bulky powder alloys were first annealed for 30 min and 12 h to form partial and complete phase-separated structures, respectively. For the ex-situ experiment, the firstly-FIB-thinned alloy specimen was prepared by FIB milling (JEOL-9420, Japan) of 30-KeV Ga ions. The firstly-FIB-thinned specimen was annealed for only 10 min at 400 ℃ to observe its phase-separation behavior.

2.2 Transmission electron microscopy

The morphologies of the three kinds of specimens were investigated by a field emission microscope (JEOL JEM-2100F) operated at 200kV. The atomic analyses (HRTEM and HAADF) and energy dispersive X-ray spectroscopy (EDS) mapping of specimens were carried out in a JEOL JEM-200ARMF equipped with double Cs-correctors and a Schottky-filed emission gun. To highlight the lattice fringes in the atomic HAADF-STEM images, the images were processed by a smooth–filter which is freely available as a plug-in for the DigitalMicrograph.[37] The Fast Fourier transformation (FFT) patterns were also obtained using the DigitalMicrograph software package (Gatan, Pleasanton, CA). The lattice strain maps were calculated from HAADF-STEM images by a geometric phase analysis (GPA) plug-in[38]. HAADF-STEM simulations were performed using the Dr.probe software,[39] implementing the multislice method to calculate the quasielastic forward scattering of the incident high-energy electron probes from the sample.

3. Results and discussion

3.1 Epitaxial relationship in the self-assembled Pt/CeO_2 nanocomposites

As reported in our previous work,[32] phase-separation and self-assembly in oxidized Pt_5Ce alloy leads to an interwoven structure of Pt and CeO_2. Atomic STEM characterizations of the Pt/CeO_2 nanocomposites annealed for 12h at 400℃ are shown in Figure 1. In the nanostructure, the bright-contrast phase of Pt

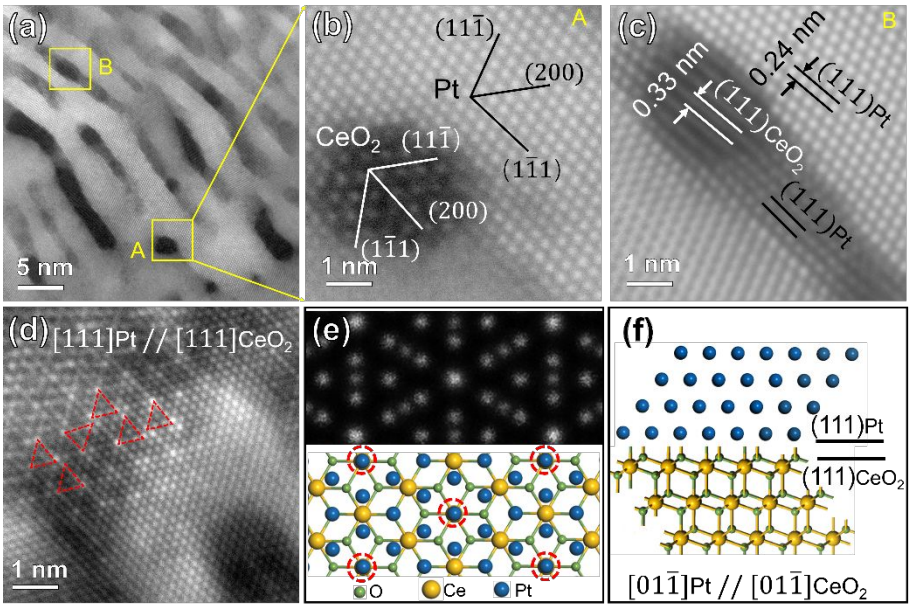

Figure 1. (a) HAADF−STEM image of the Pt_5Ce bulk sample annealed at 400℃ for 12 h showing the completely separated Pt/CeO_2 composites. (b)−(c) Enlarged filtered HAADF−STEM images of the boxes in (a), indicating the incoherent relationship between Pt and CeO_2. (d) HAADF−STEM image of another site on the same sample showing the epitaxial relationship in the [111] zone axis. (e) Schematic of the 4:3 lattice structure of $(111)_{CeO_2}$ on $(111)_{Pt}$ (top view) and the corresponding simulated HAADF−STEM image, revealing that the bright spots connected by red dashed triangles in (d) are produced by overlapped Pt and Ce atoms. (f) Side view along the [01-1] direction of the Pt/CeO_2 epitaxial interface, which has a 60° rotational relation with $(111)_{Pt}//(111)_{CeO_2}$.

alternated with the dark-contrast phase of CeO_2 (Figure 1[a]), as confirmed by the EDS mapping shown in Figure S1. The average periodicity of approximately 50 stripe structures was 4.6 nm (see histogram in Figure S2(a) for details). To clarify the orientation relationship between the Pt and CeO_2 structures, the heterointerfaces between the two phases enclosed in boxes A and B in Figure 1(a) are magnified in Fig. 1 (b) and (c), respectively. As shown in Figure 1(b), the Pt and CeO_2 crystals were exactly on the [110] zone axis but the interface was incommensurate. The angle between the (200) planes of Pt and CeO_2 was approximately 57° and the (1-11)$_{CeO_2}$ and (11-1)$_{Pt}$ planes were almost parallel. Figure 1(c) consolidates the parallel relationship between the (111) planes of Pt and CeO_2 crystals on different zone axis. Due to the lattice misfit (~38 %), several edge dislocations were found at the heterointerface. However, the relationship was fully epitaxial along the direction of the [111] zone axis (see Figure 1[d]). The brightest spots (connected by red triangles in Figure 1[d]) were deduced as overlapped Pt and Ce atoms. More specifically, the calculated lattice-constant ratio between (111)$_{CeO_2}$ and (111)$_{Pt}$ was 1.38, between the verified lattice constant ratio of 4:3 and 7:5.[40] The lower and upper parts of Figure 1(e) present a structural model of the observed structure based on the calculated 4:3 CeO_2/Pt model and a simulated HAADF–STEM image along the [111] direction, respectively. The simulation results confirm that the Pt and Ce atoms overlapped at the brightest projection spots (enclosed by the dashed red circles in the model). Integrating the relationships observed in Figure 1 (b)–(d), the lattice-matching relationship between Pt and CeO_2 that maintains (111)$_{Pt}$//(111)$_{CeO_2}$ is a certain angle of rotation. From Figure 1(d), the rotation angle was deduced as 60°, that is, the orientation relationship between Pt and CeO_2 is Pt$_{(111)}$//$CeO_{2(111)}$ 60°. This kind of rotated epitaxial relationship was already reported in thin-layers of Rh/CeO_2[41], MoS_2/S[42,43], etc., but firstly found in Pt/CeO_2 composites here. Owing to the sixfold symmetry axis of (111) planes, a 60° rotation of (111)$_{Pt}$ plane parallel to a (111)CeO_2 plane retains the epitaxial relationship, but other planes are crystallographically non-equivalent. Figure 1 (f) illustrates the side view along [01-1] direction of the structure model in Fig. 1(e). The atomic arrangement between Pt and CeO_2 matches that of Figure 1(b). Since the fully epitaxial Pt$_{(111)}$/$CeO_{2(111)}$ and the epitaxial type of Pt$_{(111)}$/$CeO_{2(111)}$ 60° are much similar in the atomic arrangement at the metal-oxide interface perimeter that plays a central role in catalysis, no prominent difference would be expected on the performance.

3.2 Phase separation behavior during the oxidation of Pt_5Ce alloy

How the special epitaxial relationship of (111)$_{Pt}$//(111)$_{CeO_2}$ with a 60° rotation evolves in the self-assembled Pt/CeO_2 composites must be elucidated. For this purpose, we prepared a partially oxidized powder specimen containing the reaction interface between the Pt_5Ce precursor and the phase-separated Pt/CeO_2 nanocomposites. By analyzing the reaction interface structure, we can understand the early stage of the phase-separation behavior. Figure 2(a) displays HAADF–STEM image of the powder precursor heated for 30 minutes, projected along the [0001]$_{Pt_5Ce}$ direction. The reaction interface between the upper Pt_5Ce alloy and lower Pt/CeO_2 nanocomposites is marked by the black dashed line. The corresponding FFT images of two regions enclosed in the yellow-edged squares are shown on the right side of Figure 2(a). These images clarify the different crystal structures of the alloy and nanocomposite. In the Pt_5Ce precursor, a periodical compositional contrast is visible within 10–20 nm from the interface. All spots in the FFT image were attributable to the Pt_5Ce structure, confirming the absence of precipitates; that is, the contrast was caused by atomic segregation. Meanwhile, the nanocomposites presented stripy patterns with alternating dark CeO_2 and bright Pt. The periodicity of the stripes was 4.6 nm, identical to that in the completely phase-separated nanocomposites. The statistical data are displayed in Figure S2 (b). It appears that the periodicity of the separated phase is independent of the annealing duration. Focusing on the near-interface region, one observes that CeO_2 stripes in the composites were connected with the dark-contrast phase in the precursor alloy. Moreover, the stripes were almost perpendicular to the reaction interface, indicating that the nanocomposites growth pointed toward the reaction interface (white arrows in the Fig. 2[a]). The Pt and CeO_2 structures viewed from the [-112] direction were identified by indexing the FFT pattern of the nanocomposites. Evidently, the Pt and CeO_2 grains shared a fully epitaxial relationship, unlike that of the completely oxidized sample [(111)$_{Pt}$//(111)$_{CeO_2}$ 60°]. The orientation relationship between the Pt_5Ce alloy and self-assembled nanocomposites was derived as (1-100)$_{Pt_5Ce}$//(220)$_{Pt/CeO_2}$, [0001]$_{Pt_5Ce}$//[-112]$_{Pt/CeO_2}$. This

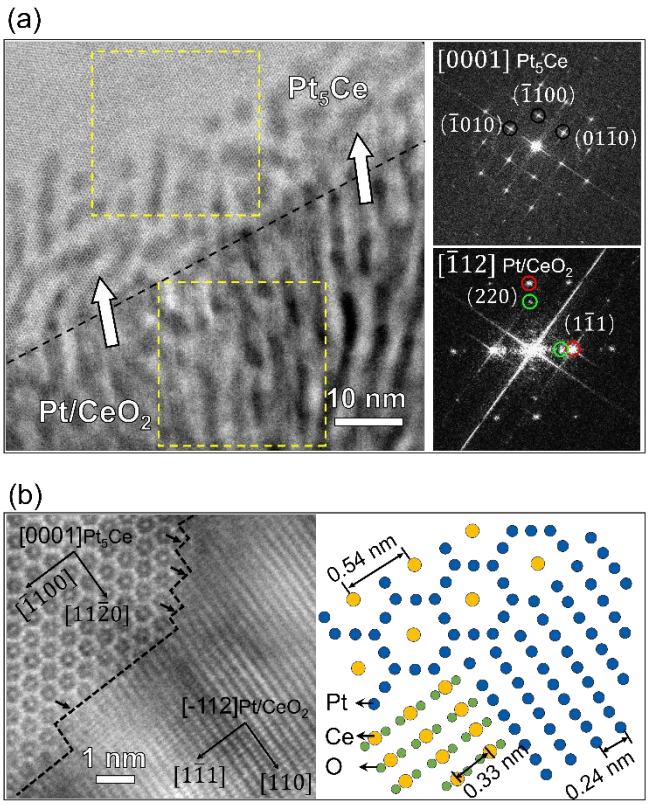

Figure 2. (a) HAADF–STEM image of the Pt_5Ce bulk sample annealed at 400°C for 30 min showing the interface area between the Pt_5Ce alloy and Pt/CeO_2 composites. The two FFT images were calculated in the areas within the yellow frames. In front of the dashed line, the contrast was caused by the atomic segregation. (b) Higher-magnification HAADF–STEM image at the reaction interface, showing the orientation relationship between the Pt_5Ce and Pt/CeO_2 composites. Right panel shows the corresponding structure model.

result is the first observed orientation relationship between hexagonal closest packed (hcp) and face-centered cubic (fcc) structures during a phase transformation. Another pronounced feature is the growth direction of the nanocomposites, which was parallel to the [110] direction. The fast growth rate of the (220) plane in [110] direction caused the preferential orientation of the Pt and CeO_2 phases in the composites, consistent with the x-ray diffraction (XRD) result (see Figure S3). In the XRD pattern, the relative intensity of the $(220)_{Pt}$ plane was much stronger than the referenced XRD powder data [JCPDS No. 04-0802].

To clarify the reaction interface structure between the Pt_5Ce alloy and Pt/CeO_2 nanocomposites, the HAADF–STEM image was magnified at the reaction interface. The image is displayed in Figure 2(b). A hexagonal arrangement of atoms was projected along the [0001] zone axis in the Pt_5Ce structure. The reaction interface was uneven and facilitated phase separation in certain stages. The arrows indicate the terraces lying exactly on the (220) plane of the nanocomposite. Based on the above-described orientation relationship between the alloy and the precipitates, the atomistic structures of the phases were derived and are displayed in the right panel of Figure 2 (b). As shown in the structural model, the plane spacing of (11-20) in the alloy was approximately twice the plane spacings of (111) in the Pt precipitates. The lattice misfit of the (111) planes of fully epitaxial Pt and CeO_2 was calculated as 36 % against Pt crystal, similar to that of the completely oxidized sample.

When alloys containing noble metals are oxidized, the noble metal phase separates from the oxide of the less noble metal. This phase separation is driven by the large discrepancy in the oxygen affinities of the noble and non-noble constituents.[44] Unlike nanoscale alloy particles,[30] which form metal core-oxide shell structures when oxidized, the microcrystalline Pt–Ce alloy in the present study formed a spatially periodic striped pattern similar to a Turing pattern. Such periodic structures have been found in the oxidized alloys based on silver,[45] nickel,[46] and other metals undergoing internal oxidation. In this scenario, one alloy component is selectively oxidized but cannot reach the surface quickly enough to form an oxide layer.[47] Alloy diffusion is thought to be negligibly slower than the inward oxygen movement, so the oxidation process is diffusion controlled.[48] The oxide in internal oxidation reactions can be spherical, facetted crystalline, dendritic, or some other shape.[49] In the striped structure observed here, the CeO_2 precipitates were constrained in their growth direction by the cerium and oxygen supplies. Consequently, the distance of oxygen diffusion to the immobile unreacted cerium was minimal, and the separated phase grew (on average) in the direction normal to the reaction interface. As oxygen must be transported through the CeO_2 phase to reach the reaction interface and Pt and Ce have different oxygen affinities, it was inferred that oxygen dissolution into the alloy contributed to atomic segregation in front of the reaction interface. CeO_2 and Pt phases were then epitaxially formed by oxidation of the Ce-rich alloy and transformation of the Pt-rich alloy, respectively. Moreover, the Pt-CeO_2 interface facilitated the oxygen diffusion from the surface to the inner Pt_5Ce alloy[44], thereby accelerating the oxidation process. The diffusion path of each element in the alloy and oxide is schematized in Figure S4. Owing to the low misfit between the (111) plane of Pt and the (11-20) plane in Pt_5Ce alloy, the phase transformation with the described orientation relationship, namely, $(1\text{-}100)_{Pt_5Ce}//(220)_{Pt/CeO_2}$, $[0001]_{Pt_5Ce}//[\text{-}112]_{Pt/CeO_2}$, beneficially minimizes the lattice strain. In contrast, the epitaxy (111) planes of Pt and CeO_2 are largely mismatched and cannot be solely compensated by inducing misfit dislocations. As the remaining lattice strain

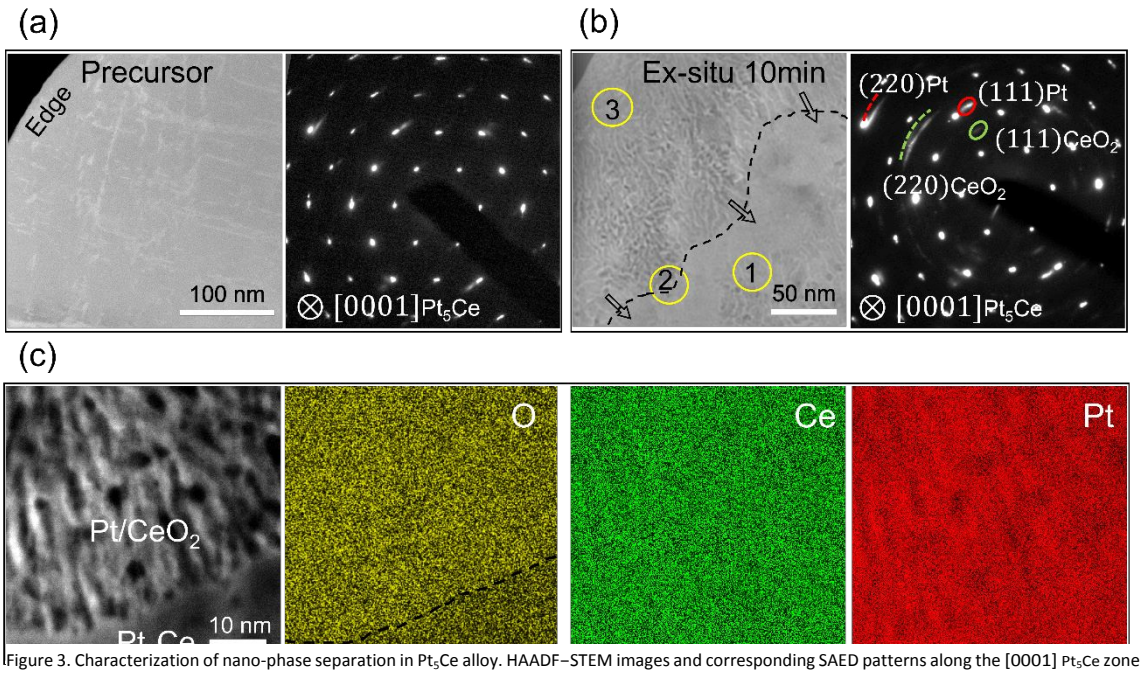

Figure 3. Characterization of nano-phase separation in Pt_5Ce alloy. HAADF–STEM images and corresponding SAED patterns along the $[0001]_{Pt_5Ce}$ zone axis of (a) Pt_5Ce alloy precursor and (b) the firstly-FIB-thinned specimen ex-situ annealed at 400℃ for 10 min. (c) HAADF–STEM image of the interface area containing the alloy precursor and separated phases, and corresponding elemental maps of O, Ce and Pt.

relaxes, the fully epitaxial relationship of Pt and CeO_2 at the early phase-separation stage should change to an epitaxial type of $(111)_{Pt}$ /$(111)_{CeO_2}$ 60° in the final stage.

3.3 Ex-situ experiment for tracking the phase-separation behavior

Although characterizing the samples prepared at different annealing times revealed the phase-separation behavior induced by oxidation, observing the whole process in a single sample would provide more conclusive results. For this purpose, we studied the phase-separation stages in an ex-situ experiment of the firstly-FIB-thinned alloy specimen. The ex-situ specimen was annealed for 10 min while the other synthesis conditions were those of the bulky powder sample.

Panels (a) and (b) of Figure 3 show the HAADF–STEM images and corresponding selected area electron diffraction (SEAD) patterns of the Pt_5Ce alloy precursor and the as-annealed alloy of the firstly-FIB-thinned specimen, respectively. The observed Pt_5Ce alloy precursor with about 300 x 300 nm^2 area presented a single hcp phase along the [0001] zone axis (Figure 3[a]) with no evidence of precipitates. After heating the initial Pt_5Ce alloy specimen ex situ to 400℃ for 10 min, two interconnected phases with stripy patterns were continuously formed from the edge of the specimen (white and gray phases in the STEM image of Figure 3[b]). In a statistical analysis of the phase-separated region, the periodicity of the two-phase stripes was determined as 4.5 nm (see Figure S2[c]). The black arrows in Figure 3(b) indicate the growth direction of the striped structure. The stripes proceeded perpendicular to the alloy interface (dashed line in the figure). The SEAD pattern showed an additional two pairs of arc-shaped reflections. Based on the calculated diffraction distances, these reflections were indexed to diffractions of the (111) and (220) planes of the Pt and CeO_2 phases. The positions of the diffraction spots suggest an almost-epitaxial relationship of the $(111)_{Pt}$ and $(111)_{CeO_2}$ planes, but with a slight swing in the same direction. Figure 3(c) shows the elemental maps of the interface-contained regions. The concentrations of O atoms differed on both sides of the interface, suggesting an oxidation- induced phase separation. Within the phase-separated regions, the white and gray stripes were apparently rich in Pt and Ce, respectively, confirming that the phase-separated region is composed of Pt/CeO_2 composites.

As explained in subsection 3.2, oxidation of Pt_5Ce alloy produces not only a Ce metal oxide, but also an fcc structure of Pt metal, which emerges through a matrix phase transformation. Moreover, the (111) planes of Pt and CeO_2 shared a parallel relationship. A striped pattern with the same periodicity was observed both in the bulky powder sample and the firstly-FIB-thinned sample, suggesting that the metal atoms diffused laterally regardless of the sample geometry. In the present case, the absence of the oxide layer at the surface further verified the slow diffusion of alloy components and the resulting predominant oxidant diffusion. Because oxidation started at the surface and progressed inward, the front and back positions (marked as positions 1 and 3 in Figure 3(b), respectively) at the interface should indicate the initial and late phase-separation stages, respectively. Therefore, to extract more information on the oxidation-induced phase-separation behavior, three regions at different separation stages (enclosed within the yellow-edged circles in Figure 3[b]) were further analyzed by HRTEM and HAADF–STEM.

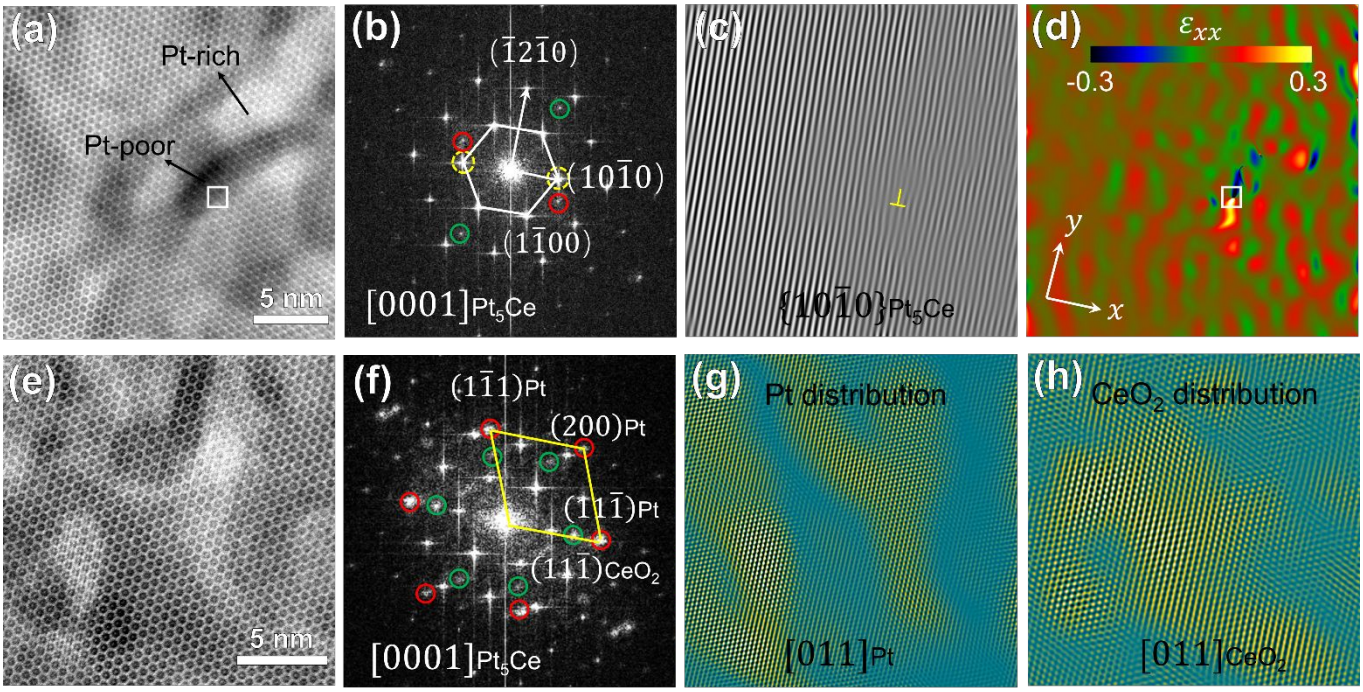

Figure 4. (a) HAADF–STEM image of the initial separation stage (region 1 in Figure 1[b]) showing atomic segregation along the $[0001]_{Pt_5Ce}$ axis, (b)FFT pattern of (a), (c) IFFT image of Pt_5Ce (10-10) extracted from (b) to highlight the lattice fringe image along $\{10\text{-}10\}_{Pt_5Ce}$ (yellow symbol indicates the edge dislocation), and (d) strain component ε_{xx} of (a) obtained in a GPA analysis: $x \parallel [10\text{-}10]_{Pt_5Ce}$, $y \parallel [1\text{-}210]_{Pt_5Ce}$. (e) HAADF–STEM image of another site in region 1 of panel 4(b), showing the Pt and CeO_2 crystals with a $[0001]_{Pt_5Ce}$ zone axis, and (f) corresponding FFT pattern (red- and green-edged circles enclose diffraction spots from the Pt and CeO_2 phases, respectively). (g) and (h) IFFT images displaying the Pt and CeO_2 distributions, obtained by extracting the six red circles and six green circles in (f), respectively.

Figure 4(a) is a HAADF–STEM image of the initial separation stage corresponding to Region 1 in Figure 3(b). The Pt-rich and Pt-poor nanoclusters are distinguished by their Z-contrast intensities. Figure 4(b) displays the corresponding FFT patterns along the [0001] orientation of the Pt_5Ce alloy precursor. Besides the reflections of Pt_5Ce, two pairs of weak reflections suggested an ordering of the nanoclusters. The inverse-FFT (IFFT) patterns of both pairs of reflections confirmed their emergence in different regions (see Figure S5). The spots enclosed by the green- and red-edged circles in Figure 4(b) were identified as CeO_2 and Pt-rich alloys, respectively. After extracting the $\{10\text{-}10\}_{Pt_5Ce}$ reflections (enclosed by the yellow-edged circles in Figure 4[b]), an edge dislocation was identified in the {10-10} plane (Figure 4[c]). This dislocation resulted from lattice distortion and strain relaxation after component segregation, which would contract or expand the lattice. To visualize the degree of lattice distortion, the local lattice strain was mapped using GPA. Figure 4(d) shows the strain component ε_{xx} of Figure 4(a). A small lattice strain appeared around the segregation areas. The obvious strain field around the edge dislocation implies a compressive strain in the Pt-poor nanoclusters and a tensile strain in the Pt-rich nanocluster, which resulted from the larger atomic radius of the Ce atoms than the Pt atoms. The compositional contrast in Figure 4(a) at the same dislocation position (white-edged square) affirms this conclusion.

Figure 4(e) shows another HAADF–STEM image in Region 1 along the $[0001]_{Pt_5Ce}$ direction. The corresponding FFT pattern in Figure 4(f) demonstrates that Pt and CeO_2 crystals were formed in the Pt_5Ce alloy. In addition to the FFT spots of Pt_5Ce alloy, spots attributed to $[011]_{Pt}$ and $[011]_{CeO_2}$ (enclosed within the red- and green-edged circles, respectively) were identified by calculating the interplanar spacings. Panels (g) and (h) of Figure 4 show the IFFT patterns determined from the Pt and CeO_2 spots in Figure 4(f), illustrating the distributions of the Pt and CeO_2 phases, respectively. The patterns re-confirm that the bright and dark contrasts in HAADF–STEM in Figure 4(e) are related to the Pt and CeO_2 phases, respectively. As the oxidation process occurred after atomic segregation, it was inferred to be governed by inward diffusion of the dissolved oxygen. Moreover, stress in the atomic segregation area promoted the oxidation[50] and phase transformation processes,[51] accelerating the penetration into the phase-separation zone.

HRTEM images of the middle and late separation stages (Regions 2 and 3 in Figure 3[b]) are displayed in Figure 5. Figure 5(a) shows the interface area of Region 2, which contains both the Pt_5Ce alloy and the phase-separated Pt/CeO_2 composites in the $[0001]_{Pt_5Ce}$ orientation. The growth direction of the Pt and CeO_2 stripes (indicated by the white arrows in Figure 5[a]) was explained earlier. In the corresponding FFT pattern (Figure 5[b]), the red and green-edged circles mark the Pt and CeO_2 spots, respectively. Clearly, the epitaxial relationship between Pt and CeO_2 was established in this separation stage. Moreover, the growth direction of the Pt/CeO_2 composites is consistent with the $[111]_{Pt/CeO_2}$ direction. Considering the phase transformation of Pt_5Ce alloy with an hcp structure to Pt with

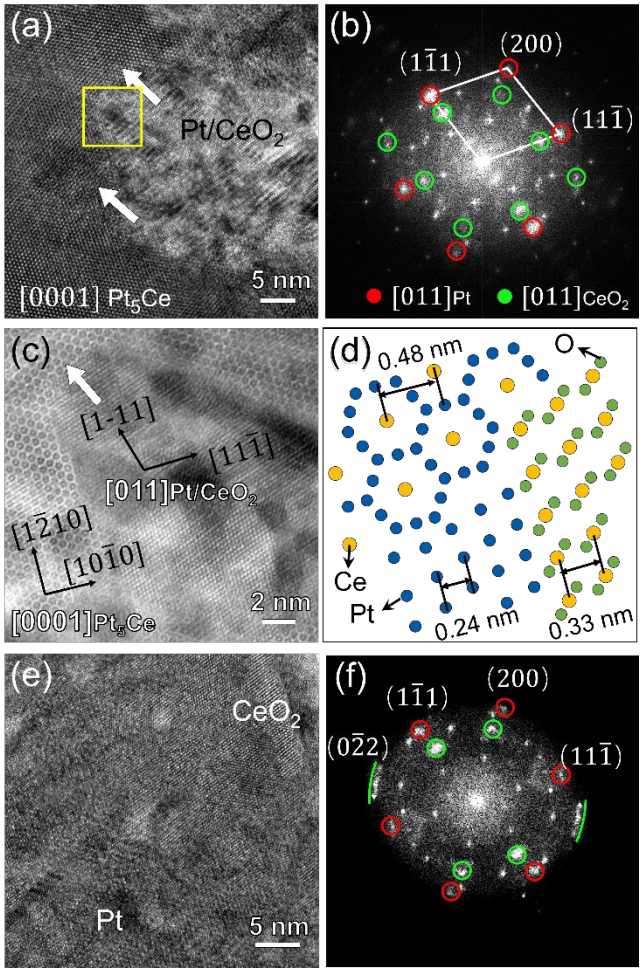

Figure 5. (a) HRTEM image with $[0001]_{Pt_5Ce}$ zone axis and (b) corresponding FFT of the middle separation stage (region 2 in Fig. 3(b)) showing the interface area between Pt_5Ce alloy and Pt/CeO_2 composites. (c) HAADF–STEM image of the boxed area in (a), and (d) atomic structure model of each phase in the interface area. (e) HRTEM image along the $[0001]_{Pt_5Ce}$ zone axis and corresponding FFT of the late separation stage (region 3).

an fcc structure, the orientation relationship between the two phases was obtained as $\{10\text{-}10\}_{Pt_5Ce}//(1\text{-}11)_{Pt/CeO_2}$, $[0001]_{Pt_5Ce}//[011]_{Pt/CeO_2}$, which differs from the typically reported phase relationship in Pt_5Ce surface alloy transformation, i.e., $\{0001\}_{Pt_5Ce}//\{111\}_{Pt}$.[28] Figure 5(c) is an enlarged atomic STEM image of the region enclosed by the square in Figure 5(a). This image confirms the above-derived orientation relationships between the Pt_5Ce alloy and the Pt/CeO_2 composites. The atomic structure model of phase separation in this system is shown in Figure 5(d). In the direction nearly normal to the growth direction of the precipitates, the lattice spacing of the (10-10) plane of the Pt_5Ce alloy was twice that of the (111) plane of Pt crystals. This perfect alignment favors phase separation. In the (111) planes, the ratio of the Pt to CeO_2 lattice vectors was 1.38 with an approximate misfit of 38%. Judging from the large misfit at the coherent interface, the epitaxial relationship between Pt and CeO_2 was probably unstable to further reactive heating.

In the late separation stage (close to the edge of the thinned specimen, indexed as Region 3 in Figure 3[b]), the situation was somewhat different. The HRTEM image of this phase-separated area is shown in Figure 5(e). The composite

structure of Pt and CeO_2 is clearly visible. The corresponding FFT image is displayed in Figure 5(f). Comparing the reflections in panels (b) and (f) of Figure 5, we find that some reflection spots developed arc shapes in the late separation stage and the CeO_2 crystals were shifted from the correct zone axis. The reflections from CeO_2(11-1) disappeared while those from (220) were stronger than those in the interface area. It was deduced that during the growth process, the CeO_2 crystals rotated through a small angle while the epitaxial relationship was retained on the (111) planes. Such rotational behavior is often found in largely mismatched metal–oxide heterointerface systems because it lowers the interface energy.[52,53] Given the large misfit between the Pt and CeO_2 phases (38%), the crystal rotation was likely enforced by strain relaxation.

Based on the above results, the phase-separation behavior in the present samples was identical to that found in bulky powder samples and proceeded in three steps. In the first step, atomic segregation of Pt and Ce in the Pt_5Ce alloy because of their different oxygen affinity. As the oxygen continues to diffuse into the Ce-rich regions, the self-assembled Pt and CeO_2 stripy phases with a fully epitaxial relationship then become separated from the alloy during the early stage. Owing to the large misfit between the lattice constants of Pt and CeO_2 phases, the crystals with an initially commensurate interface tend to rotate along [111], and finally maintain the $(111)_{Pt}//(111)_{CeO_2}$ relation. The phase-separation behavior is schematized in Fig. S6. It should be noted that although stripy patterns of Pt and CeO_2 are kinetically favorable to minimize the oxygen diffusion distance to the immobile unreacted cerium, the stripes growth direction and the orientation relationship between the stripes and the precursor alloy should be energetically favorable because of the large internal surface area. Therefore, the preferred growth direction and orientation of stripes vary with the orientation of the precursor alloy and annealing temperature. Moreover, different growth directions ([110] and [111], respectively) and orientation relationships (see stereographic projections in Figure S7) in the bulky powder and firstly-FIB-thinned specimens indicate the influence of the oxygen partial pressure for the phase separation behavior. This is because oxygen can more easily reach the reaction interface on the surfaces of FIB-thinned samples than the inside bulky powder samples. The stripes were assumed to be oriented perpendicular to the growing interface between the alloy and Pt/CeO_2 precipitants; accordingly, the growth direction is closely related to the orientation relationship between Pt_5Ce and Pt/CeO_2.

4. Conclusions

Self-assembled epitaxial interfaces of Pt/CeO_2 nanocomposites were successfully formed by simple oxidation of Pt_5Ce alloy. Nanoscale stripy patterns of alternating Pt and CeO_2 phases were observed and an epitaxial interface between Pt and CeO_2 was identified on their (111) planes. Furthermore, the oxidation-induced phase-separation process in a partially oxidized sample was observed by atomic-scale TEM, and a verification experiment was performed by ex-situ annealing of a firstly-FIB-thinned TEM specimen. The oxygen partial pressure on the surface of the FIB-thinned specimen differed from that inside bulky powder samples, affecting the growth direction of the stripes and the orientation relationship between the Pt_5Ce alloy and Pt/CeO_2 composites. These findings suggest that Pt/CeO_2 catalysts with an epitaxial interface can be economically prepared for fundamental research and practical applications. Furthermore, our results are expected to assist the structural design of metal–oxide nanocomposites.

Author contributions

Yu Wen: conceptualization, methodology, formal analysis, writing-original draft; Hideki Abe: funding acquisition, writing-review & editing; Kazutaka Mitsuishi: writing-review& editing; Ayako Hashimoto: conceptualization, supervision, funding acquisition, writing-review& editing.

Conflicts of interest

There are no conflicts to declare.

Acknowledgements

This work was funded by the Precursory Research for Embryonic Science and Technology (PREST) (Grant No. JPMJPR17S7) and Core Research for Evolutional Science and Technology (CREST), Japan. We thank TEM station of National Institute for Materials Science (NIMS) for the support of using TEM and EDS techniques.

Notes and references

1. S. Park, J. M. Vohs and R. J. Gorte, *Nature*, 2000, **404**, 265–267.
2. M. Takahashi, T. Mori, F. Ye, A. Vinu, H. Kobayashi and J. Drennan, *J. Am. Ceram. Soc.*, 2007, **90**, 1291–1294.
3. C. Sun, H. Li and L. Chen, *Energy Environ. Sci.*, 2012, **5**, 8475–8505.
4. L. Sun, D. Marrocchelli and B. Yildiz, *Nat. Commun.*, 2015, **6**, 1–10.
5. S. A. Acharya, V. M. Gaikwad, V. Sathe and S. K. Kulkarni, *Appl. Phys. Lett.,* 2014, **104**, 113508.
6. D. R. Mullins, P. M. Albrecht, T. L. Chen, F. C. Calaza, M. D. Biegalski, H. M. Christen and S. H. Overbury, *J. Phys. Chem. C*, 2012, **116**, 19419–19428.
7. K. Werner, X. Weng, F. Calaza, M. Sterrer, T. Kropp, J. Paier, J. Sauer, M. Wilde, K. Fukutani, S. Shaikhutdinov and H. J. Freund, *J. Am. Chem. Soc.*, 2017, **139**, 17608–17616.
8. Y. Huang, B. Long, M. Tang, Z. Rui, M. S. Balogun, Y. Tong and H. Ji, Appl. Catal. B Environ., 2016, 181, 779–787.
9. Y. Huang, Y. Lu, Y. Lin, Y. Mao, G. Ouyang, H. Liu, S. Zhang and Y. Tong, J. Mater. Chem. A, 2018, 6, 24740–24747.
10. J. Yang, N. Xie, J. Zhang, W. Fan, Y. Huang and Y. Tong, Nanomaterials, 2020, 10, 1–12.
11. D. Gao, Y. Zhang, Z. Zhou, F. Cai, X. Zhao, W. Huang, Y. Li, J. Zhu, P. Liu, F. Yang, G. Wang and X. Bao, *J. Am. Chem. Soc.*, 2017, **139**, 5652–5655.
12. Z. Lu and Z. Yang, *J. Phys. Condens. Matter*, 2010, **22**, 475003.
13. J. A. Rodriguez, D. C. Grinter, Z. Liu, R. M. Palomino and S. D. Senanayake, *Chem. Soc. Rev.*, 2017, **46**, 1824–1841.
14. M. Boudart, *Adv. Catal.,* 1969, **20**, 153–166.
15. Q. Fu, H. Saltsburg and M. Flytzani-Stephanopoulos, *Science*, 2003, **301**, 935–938.
16. H. H. Liu, Y. Wang, A. P. Jia, S. Y. Wang, M. F. Luo and J. Q. Lu, *Appl. Surf. Sci.*, 2014, **314**, 725–734.

17. H. P. Zhou, H. S. Wu, J. Shen, A. X. Yin, L. D. Sun and C. H. Yan, *J. Am. Chem. Soc.*, 2010, **132**, 4998–4999.
18. C. Spiel, P. Blaha, Y. Suchorski, K. Schwarz and G. Rupprechter, *Phys. Rev. B - Condens. Matter Mater. Phys.*, 2011, **84**, 1–11.
19. S. Aranifard, S. C. Ammal and A. Heyden, *J. Phys. Chem. C*, 2014, 118, 6314–6323.
20. W. Rong, H. Chen, Z. Huang and K. Wu, *J. Phys. Chem. C*, 2020, **124**, 6284–6289.
21. C. Xu, Y. Wu, S. Li, J. Zhou, J. Chen, M. Jiang, H. Zhao and G. Qin, *J. Mater. Sci. Technol.*, 2020, **40**, 39–46.
22. Y. Gao, W. Wang, S. Chang and W. Huang, *ChemCatChem*, 2013, **5**, 3610–3620.
23. M. Cargnello, V. V. T. Doan-Nguyen, T. R. Gordon, R. E. Diaz, E. A. Stach, R. J. Gorte, P. Fornasiero and C. B. Murray, *Science*, 2013, **341**, 771–773.
24. L. Tao, Y. Shi, Y. Huang, Y. Zhang, J. Huo, Y. Zou, J. Luo, C. Dong and S. Wang, *Nano Energy*, 2018, **53**, 604–612.
25. H. Iida, A. Igarashi, *Appl. Catal. A Gen*, 2006,**298**, 152–160.
26. M. Sedighi, A. A. Rostami and E. Alizadeh, *Int. J. Hydrogen Energy*, 2017, **42**, 4998–5005.
27. Y. Kozu, S. Kawashima and F. Kitamura, *J. Solid State Electrochem.*, 2013, **17**, 761–765.
28. U. Berner and K. D. Schierbaum, *Phys. Rev. B - Condens. Matter Mater. Phys.*, 2002, **65**, 2354041–23540410.
29. C. Hardacre, T. Rayment and R. M. Lambert, *J. Catal.*, 1996, **158**, 102–108.
30. E. A. Sutter, X. Tong, K. Jungjohann and P. W. Sutter, *Proc. Natl. Acad. Sci. U. S. A.*, 2013, **110**, 10519–10524.
31. P. Sutter, S. A. Tenney, F. Ivars-Barcelo, L. Wu, Y. Zhu and E. Sutter, *Nanoscale Horizons*, 2016, **1**, 212–219.
32. Y. Wen, A. Hashimoto, A. S. B. M. Najib, A. Hirata and H. Abe, *Appl. Phys. Lett.*, 2020, **118,** 054102.
33. T. Tanabe, T. Imai, T. Tokunaga, S. Arai, Y. Yamamoto, S. Ueda, G. V. Ramesh, S. Nagao, H. Hirata, S. I. Matsumoto, T. Fujita and H. Abe, Chem. Sci., 2017, 8, 3374–3378.
34. T. Imai, S. Ueda, S. Nagao, H. Hirata, K. R. Deepthi and H. Abe, RSC Adv., 2017, 7, 9628–9631.
35. A. S. Bin Mohd Najib, X. Peng, A. Hashimoto, S. Shoji, T. Iida, Y. Bai and H. Abe, Chem. – An Asian J., 2019, 14, 2802–2805.
36. A. S. Bin Mohd Najib, M. Iqbal, M. B. Zakaria, S. Shoji, Y. Cho, X. Peng, S. Ueda, A. Hashimoto, T. Fujita, M. Miyauchi, Y. Yamauchi and H. Abe, J. Mater. Chem. A, 2020, 8, 19788–19792.
37. Dave Mitchell's DigitalMicrograph™ Scripting Website. http://www.dmscripting.com/hrtem_filter.html.
38. Useful Plugins and Scripts for DigitalMicrograph. https://www.physik.hu-berlin.de/en/sem/software/software_frwrtools.
39. J. Barthel, Ultramicroscopy, 2018, 193, 1-11.29. F. H. Stott and G. C. Wood, *Mater. Sci. Technol.*, 1988, **4**, 1072–1078.
40. C. Spiel, P. Blaha, Y. Suchorski, K. Schwarz and G. Rupprechter, *Phys. Rev. B - Condens. Matter Mater. Phys.*, 2011, **84**, 045412.
41. S. Bernal, F. J. Botana, J. J. Calvino, G. A. Cifredo, J. A. Pe´rez-Omil and J. M. Pintado, Catal. Today, 1995, **23**, 219–250.
42. Q. Ji, M. Kan, Y. Zhang, Y. Guo, D. Ma, J. Shi, Q. Sun, Q. Chen, Y. Zhang and Z. Liu, Nano Lett., 2015, 15, 198–205.
43. N. Marzari, O. L. Sanchez, Y. Kung, D. Krasnozhon, M. Chen, S. Bertolazzi, P. Gillet, A. Fontcuberta, A. Radenovic and A. Kis, ACS Nano, 2015, 4, 4611–4620.
44. G. C. Wood and F. H. Stott, *Mater. Sci. Technol.*, 1986, **3**, 519–530.
45. T. D. Nguyen, J. Zhang and D. J. Young, *Corros. Sci. Technol.*, 2015, **14**, 127–131.
46. D. T. M. Do and M. Nanko, *Mater. Sci. Forum*, 2011, **696**, 384–388.
47. D. J. Young, *Defect Diffus. Forum*, 2012, **323-325**, 283-288.
48. F. H. Stott and G. C. Wood, *Mater. Sci. Technol.*, 1988, **4**, 1072–1078.
49. D. J. Young, *High Temperature Oxidation and Corrosion of Metals: Second Edition*, Corrosion series, Sydney, 2nd edn., 2008.
50. H. E. Evans, *Int. Mater. Rev.*, 1995, **40**, 1–40.
51. D. H. Hong, T. W. Lee, S. H. Lim, W. Y. Kim and S. K. Hwang, *Scr. Mater.*, 2013, **69**, 405–408.
52. K. Matsunaga, T. Sasaki, N. Shibata, T. Mizoguchi, T. Yamamoto and Y. Ikuhara, *Phys. Rev. B - Condens. Matter Mater. Phys.*, 2006, **74**, 2–9.
53. F. Ernst, *Mater. Sci. Eng. R*, 1995, **14**, 97–156.